

PAPER

Electroluminescence transients and correlation with steady-state solar output in solution-prepared $\text{CH}_3\text{NH}_3\text{PbI}_3$ perovskite solar cells using different contact materials

To cite this article: M Córdoba *et al* 2020 *J. Phys. D: Appl. Phys.* **53** 115501

View the [article online](#) for updates and enhancements.

You may also like

- [Electroluminescence at the n-ZnO / Electrolyte Interface: A Comparative Study of the Emission Processes under Cathodic and Anodic Pulsed Polarization](#)
Denis Fichou and Jean Kossanyi
- [PhotoElectroluminescence in Commercial ThinFilm Electroluminescent Panels](#)
R. G. Pappalardo
- [Red Electroluminescence of Mn-doped CuAlS₂ Powder and Single Crystal](#)
Katsu Tanaka, Yasukazu Kimura, Shinji Okamoto *et al.*



The Electrochemical Society
Advancing solid state & electrochemical science & technology

241st ECS Meeting

May 29 – June 2, 2022 Vancouver • BC • Canada

Abstract submission deadline: Dec 3, 2021

Connect. Engage. Champion. Empower. Accelerate.
We move science forward



Submit your abstract



Electroluminescence transients and correlation with steady-state solar output in solution-prepared $\text{CH}_3\text{NH}_3\text{PbI}_3$ perovskite solar cells using different contact materials

M Córdoba^{1,2}, W Herrera^{3,4}, A Koffman-Frischknecht^{2,5}, N Correa^{3,4},
M D Perez^{3,4} and K Taretto^{1,2} 

¹ Departamento de Electrotecnia (FAIN-UNCo), Buenos Aires 1400, (8300) Neuquén, Argentina

² Instituto de Investigación y Desarrollo en Ingeniería de Procesos, Biotecnología y Energías Alternativas (PROBIEN, CONICET-UNCo), Buenos Aires 1400, (8300) Neuquén, Argentina

³ Departamento Energía Solar, GIyA, Centro Atómico Constituyentes, CNEA, CONICET, Av. Gral. Paz 1499, (1650) San Martín, Buenos Aires, Argentina

⁴ Instituto de Nanociencia y Nanotecnología, CNEA-CONICET, Centro Atómico Constituyentes, Av. Gral. Paz 1499, (1650) San Martín, Buenos Aires, Argentina

⁵ Departamento de Física (FAIN-UNCo), Buenos Aires 1400, (8300) Neuquén, Argentina

E-mail: kurt_taretto@yahoo.com

Received 10 October 2019, revised 3 December 2019

Accepted for publication 11 December 2019


Published 3 January 2020



Abstract

Electroluminescence (EL) **transients** of solution-prepared $\text{CH}_3\text{NH}_3\text{PbI}_3$ perovskite solar cells were recorded **under different biasing voltage conditions**. The EL transients are reversible and show a **sharp increase and a peak in the range of 1 s to 10 s**, while after the **peak the signal decays in 30 s to 60 s**. The possible origins of the different features are discussed, pointing to a shift in the region of dominating recombination during biasing, governing the EL increase, and the creation of ion migration-induced non-radiative recombination centers during the EL decrease. Moreover, when **ramping up the polarization voltage**, the **EL transients shorten**, suggesting an acceleration of the microscopic mechanism with increasing electric fields. Cells prepared with compact instead of mesoporous TiO_2 electron contact **show faster dynamics**, highlighting the link between dynamics and interface properties. Furthermore, experiments using cells with different hole contacts show that the observed behavior and the duration of the transient is similar in cells using Spiro-OmeTAD and copper phthalocyanine (CuPc). When considering the steady-state EL, the open circuit voltage under solar operation correlates with EL across samples with different HTL materials. A non-monotonous behavior is also observed in temperature-dependent EL transients, where maxima in EL as well as in time to the peak are observed around 30 °C, which is close to the temperature of crystalline phase change from tetragonal to cubic phase known in $\text{CH}_3\text{NH}_3\text{PbI}_3$ at 37 °C.

Keywords: solar cells, perovskite, electroluminescence, transient response, optoelectronic reciprocity

 Supplementary material for this article is available [online](#)

(Some figures may appear in colour only in the online journal)

1. Introduction

Perovskite solar cells (PSC) are at the pinnacle of the efforts directed to the development of third generation photovoltaics, highly regarded as top candidates for near term massive impact on renewable energy production [1]. Despite the fast progress towards highly efficient and durable devices achieved by the scientific community, the complexity of PSC demands a diverse set of characterization methods and models to disentangle microscopic phenomena [2]. It is expected that a greater knowledge of the underlying mechanisms will pave the way to the development of new preparation methods and materials for production-ready devices [3].

A widespread tool in the characterization of solar cells in scientific laboratories as well as photovoltaic modules in industrial production is the electroluminescence (EL) imaging technique [4–6]. Using a simple setup composed by a CCD camera and a power source, EL imaging records the light emitted by the photovoltaic device in the dark upon biasing and current injection [6]. Owing to a correspondence between dark and illuminated characteristics, the features revealed in EL images are directly linked to the device under solar illumination [5], rendering EL imaging as a reliable and fast characterization technique for solar devices in general. In PSC, EL constitutes a valuable technique, already proven successful for the characterization of layer homogeneity and localization of degradation spots [7, 8]. However, the general use of EL in PSC requires careful inspection, since many PSC solar cell architectures show a time-dependent response, most widely revealed by the well-known rate-dependent hysteresis observed in current–voltage characterization [9]. The timescale of transient behavior in PSC spans from the microsecond to the hour range, with several different microscopic phenomena ruling each transient phase, from fast charge injection (in the order of ns), migration of fast ions (ms), interface charge/discharge (up to 10 s), and slow ion migration (1000 s) [10, 11]. Although screening EL as a fast tool, such long lasting transients may offer a complementary method to the characterization under solar operation. In previous investigations, EL transients were recorded in lead-halide PSC, showing a monotonous increase towards a stationary value in the minute scale [12], where others observed a non-monotonous evolution showing a maximum at timescales of up to 25 min, followed by a slower decrease [13]. In a recent paper [14], Wong *et al* employed EL transient characterization across solar cells prepared with different electron contacts, finding important differences in the different EL decay rates depending on the chosen electron contact materials. This allowed to estimate the amount of non-radiative recombination at the defect energy levels at the interfaces of each device introduced by each material. Such analyses can be expanded when incorporating other variables, for instance the relative EL intensity difference across samples, the link between transient EL and steady-state solar output characteristics, and the temperature dependence of EL.

In this contribution, we report the systematic EL transient characterization of methylammonium lead iodide ($\text{CH}_3\text{NH}_3\text{PbI}_3$ or MAPI for short) solar cells, focusing on the

characteristic times, the EL intensity relative to the injected current, and the relationship between the EL characteristics and the open-circuit voltage under solar operation. We analyze in detail different shapes of the EL transients under several polarization conditions in solar cells using different electron as well as hole contacts, revealing the impact of interfacial recombination introduced by each contact material, and finding a correlation between solar cell output and EL transients across cells. Moreover, temperature dependent EL transients show a non-monotonous behavior which possibly reflects the occurrence of a change in crystalline phase near room temperature. The paper structure is as follows: section 2 describes the experimental methods employed during the preparation and characterization of the samples, detailing the procedure followed during EL recording. Section 3 presents the results, showing first a typical EL image time-sequence with the resulting EL transient curves defining characteristic transient parameters, outlining the possible origin of the observed behavior. The characteristic parameters are later linked to the solar output parameters and compared across devices with different contact materials. The last part of section 3 shows temperature dependent experiments, where the EL transients reveal a maximum that is associated to structural transitions.

2. Experimental methods

2.1. Solar cell preparation

The FTO glass substrates were cleaned with detergent and Milli-Q water in an ultrasound for 10 min, followed by immersion in acetone, ethanol and isopropyl alcohol for 10 min. The substrates were blow-dried under N_2 flow and finally exposed to air plasma for 7 s. The compact TiO_2 layer was deposited by spin coating at 2000 rpm for 20 s from a solution of TiCl_4 in ethanol 1:200. In the case of cells using a porous layer, after thermal annealing the compact TiO_2 at 100 °C for 10 min, a mesoporous TiO_2 layer was deposited by spin coating at 2000 rpm for 20 s from a 5% vol TiO_2 paste (Greatcell Solar 30NR-D) in ethanol. Finally, the films were sintered at 500 °C for 30 min. High-quality perovskite thin films were obtained by the one-step method, using a 1:1:1:1 stoichiometric relation. Lead iodide PbI_2 99.995% (Beantown Chemical) was completely dissolved in a solution mixture of DMSO and DMF (Merck) with a 1:1:1 relation, and heated to 70 °C–80 °C. The Methylammonium iodide ($\text{CH}_3\text{NH}_3\text{I}$) > 99%, (Greatcell Solar) was added to the resulting solution after cooling. The resulting $\text{CH}_3\text{NH}_3\text{PbI}_3$ (MAPI) solution was filtered through a PVDF syringe filter (0.45 μm pore) and spin-coated onto the previously prepared titania film at 4000 rpm for 50 s. Chlorobenzene was applied as an antisolvent during spinning. The film was later annealed for 2 min at 100 °C on a heating plate. In the preparation of Spiro hole transporting layer, 72.3 mg of 2,2',7,7'-Tetrakis[N,N-di(4-methoxyphenyl)amino]-9,9'-spirobifluorene (Spiro-OMeTAD), 28.8 μl of tert-butylpyridine (Sigma-Aldrich), and 17.5 μl of a previously prepared solution of 520 mg ml^{-1} of lithium bis-(trifluoromethylsulfonyl) imide (Sigma-Aldrich)

in acetonitrile was dissolved in 1 ml of chlorobenzene. CuPc 40 nm hole transporting layer were prepared by thermal evaporation of copper phthalocyanine (Sigma-Aldrich), with an evaporation rate of 2 nm s^{-1} at a 10^{-5} Torr pressure. The Au electrode was thermally evaporated on HTL with the same evaporation parameters than CuPc, obtaining a layer of 130 nm.

2.2. *I–V characterization*

The current density–voltage (*JV*) curve measurements were realized under AM1.5G illumination (100 mW cm^{-2}) using an Abet SunLite 0.2 solar simulator and a Keithley 2400 source meter. In all *JV* measurements, a voltage sweep from -0.2 to 1.2 V with a scan rate of 100 mV s^{-1} was used. Figures S1 and S2 (stacks.iop.org/JPhysD/53/115501/mmedia) in the supplementary information show the *JV* curves and its parameters for samples with Spiro-MeOTAD and CuPc respectively.

2.3. *EL imaging and processing*

EL imaging was performed using a commercial infrared CCD camera (mvBlueFOX) in video mode, set at one second integration time for each frame. The EL time evolution was measured during 60 s at a frame rate of one image per second and 0.985 s integration time, immediately after biasing with a Keithley 2400 source meter operated under constant voltage mode, simultaneously tracking the injected current with a multimeter. The sample holder and camera were placed inside a dark box, also enabling the measurement of dark *JV* curves. In order to avoid polarization preconditioning between measurements, we kept the samples without polarization under dark condition during 4 min between different video acquisition events, allowing to reach electrostatic equilibrium at zero bias in the dark. The temperature-dependent measurements were performed on samples covered with a 1 mm thick glass that allowed to make physical contact using thermal conducting paste onto a Peltier-regulated temperature aluminum plate. The sample temperature was estimated as the mean value of the plate temperature, obtained through a thermocouple placed within the aluminum block ca. 1 mm below the surface, and the temperature of the top glass obtained by an infrared thermometer. The error in temperature was estimated as the average deviation of each measurement to the mean value.

3. Results and discussion

Solar cells with different performances were fabricated. Table 1 shows the forward- and reverse-scan output parameters of four MAPI-based solar cells measured under AM1.5G simulated light at room temperature. We purposely observed two devices with the same layer construction (namely Spiro-a and Spiro-b in table 1), using SpiroMeOTAD as HTL, but with different efficiencies in order to analyze the EL characteristics. Most likely, the smaller efficiency of sample Spiro-b is related to an increased light absorption and reduced electronic

properties of the Spiro layer depending on its oxidation state [13, 15].

Figure 1 shows a sequence of images of EL emission of a MAPI solar cell with Spiro-MeOTAD as the HTL, upon 1.1 V forward bias polarization. A decay in brightness is observed after the maximum brightness is achieved at 4 s (EL_{MAX}), slowly reaching a stationary EL image at ca. 20 s. The EL images reveal a certain degree of defect inhomogeneity within the entire device area. The luminescence appears brighter initially at the frontiers of the device where typical border defects are expected. It later shows a brighter zone at the top of the device at t_{MAX} that may be due to the radial distribution (which corresponds to the vertical direction in figure 1) of the material defects that are inherent from the spin coating process.

By summing up all the pixel counts of each image, we obtain the EL curve as a function of time as shown in figure 2 (black line, left y-axis), shown together with the injected forward current (red line, right y-axis). The EL signal increases towards EL_{MAX} from a starting value of about 25% of EL_{MAX} , followed by a much slower decrease towards a stationary value around 60 s. In contrast, the initial value of the injected current starts at nearly 80% of the steady state value reached at 53 s, while the EL signal continues to decrease. The time-scale in the minute-range needed to reach the stationary current seems compatible with surface polarization models that take into account the migration and release rates of ions from/towards interfaces [16]. Field-induced structural changes in the crystal lattice of MAPI may also play a role in the slow dynamics, although to a smaller degree [17]. Since the amplitude of the variation of the current is clearly smaller than the amplitude of the EL transient, we consider that the observed rise and fall of EL is only linked to a strong shift in the balance between radiative and non-radiative recombination with time, disregarding the transient of the injected current from the analysis.

Similar EL transients were observed previously in MAPI light emitting diodes having identical layer structure as our samples, and were understood by visible degradation effects upon current injection [13]. In our case, however, no appreciable degradation effects are seen after the EL transients, which are reproducible and reversible, as shown below. Therefore, it is much more likely that a change in the time-dependent radiative recombination is taking place in our measurements. Under this assumption, the observed peak-shaped EL transients must be ruled fundamentally by two counteracting mechanisms: a shift in the balance between non-radiative and radiative recombination during the first stages of biasing, and the generation of new defects that act as recombination centers with biasing time. Such defect generation upon polarization has been observed e.g. in MAPI films, where the vanishing of photoluminescence upon biasing in a coplanar contact geometry corresponds to the appearance of non-radiative recombination centers, conditioned by ion motion [18, 19]. We assume that this process of defect generation is present during the whole experiment. Contrarily, the factor that introduces the non-monotonous behavior in the EL is in our opinion the change in the band diagram. Within the typical ‘wiggly band’ [20]

Table 1. Forward and reverse short circuit current density J_{SC} , open circuit voltage V_{OC} , fill factor FF and efficiency η of four solar cells measured under AM1.5G simulated light at room temperature. The designations p-TiO₂ represent a FTO substrate cover with a compact TiO₂ layer, while m-TiO₂ refers the same substrate covered with a mesoporous TiO₂ layer.

	Area [cm ²]	Scan directions	J_{SC} [mA cm ⁻²]	V_{OC} [V]	FF [%]	η [%]
m-TiO ₂ /MAPI/Spiro-a	0.33	Backward	14.42	1.02	65.9	10.6
		Forward	14.42	0.99	55.8	7.31
m-TiO ₂ /MAPI/Spiro-b	0.27	Backward	12.05	0.91	62.6	6.88
		Forward	12.03	0.89	48.9	5.28
m-TiO ₂ /MAPI/CuPc	0.27	Backward	16.76	0.85	53.3	7.55
		Forward	17.48	0.81	28.6	4.05
p-TiO ₂ /MAPI/Spiro	0.19	Backward	3.59	0.97	51.4	1.79
		Forward	7.81	0.96	11.3	0.85

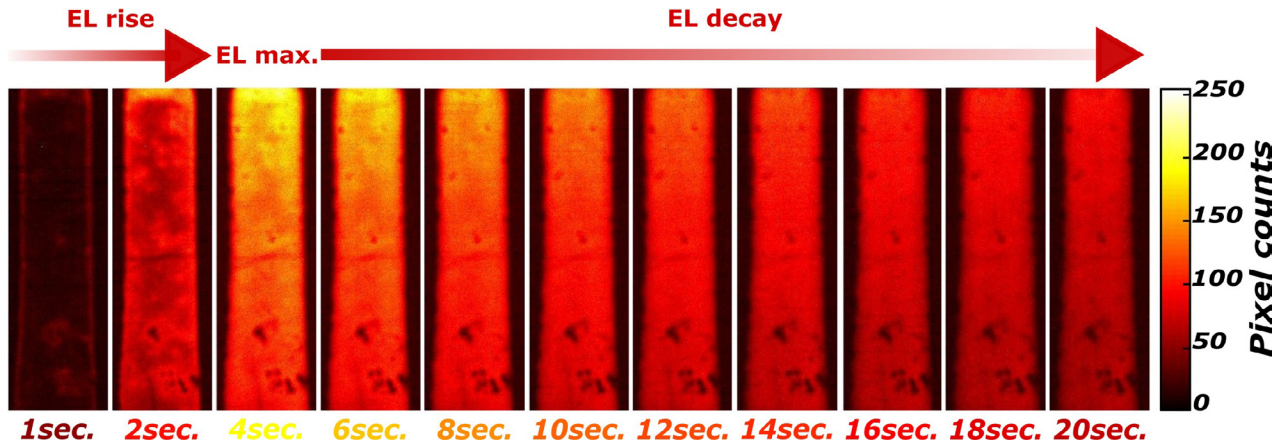


Figure 1. Time sequence showing the rise, maximum, and decay of EL images of sample m-TiO₂/MAPI/Spiro-a biased at 1.1 V. The maximum EL is observed at 4 s after polarization.

model for a MAPI solar cell, it is the central part of the perovskite layer which first absorbs the drop of the applied potential. As a consequence, the band bendings at the interfaces remain mainly unchanged, offering significant barriers for carrier injection (see scheme 3 in [20]). The barriers thus favor non-radiative recombination at the interfaces, leaving a certain initial level of radiative recombination in the perovskite. With the ongoing slow ion movement to counteract the applied potential, the band bendings at the interfaces are gradually lowered, decreasing the barriers to carrier injection. This implies that a larger portion of the injected carriers are allowed to reach the interior of the MAPI layer. Depending on the concentration of active recombination centers in the perovskite, this shift in the regions of higher recombination is capable of enhancing radiative recombination, with the resulting EL increase observed in our experiments. The aforementioned generation of defects with time counteracts the former process, leading to a reduction of charges available for radiative recombination. If defect generation is slow enough, then a peak in the EL must appear, as seen in our experiments. Such interplay of the involved stages must of course depend strongly on the interface defect concentration. Recently, EL transients in MAPI light-emitting diodes were found to show monotonous or non-monotonous behavior depending on the thickness of SnO₂ electron contact layer, highlighting the strong influence of interface properties on the observed dynamics [21]. Moreover, there are further processes that are believed to contribute to the observed EL

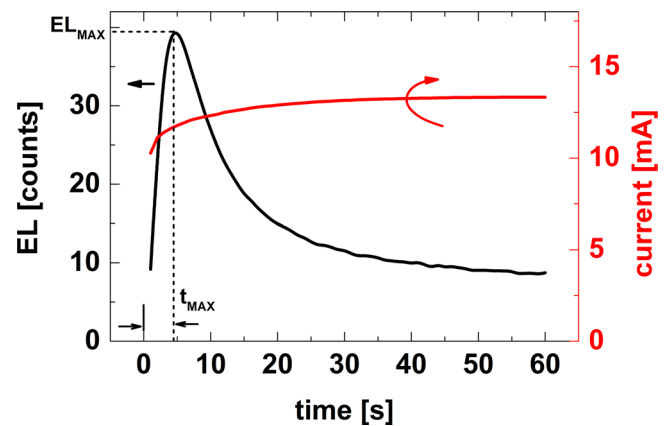


Figure 2. Typical EL intensity (left y-axis) curve as a function of time obtained by integration of EL images in sample m-TiO₂/MAPI/Spiro-a, and time dependence of injected forward current (right y-axis) at a fixed forward bias voltage of 1.1 V.

decay, such as structural changes occurring in MAPI layers during polarization [17], which include lattice distortions and changes in the interface electronic properties. We believe that further investigations including detailed experiments and modeling are required to allow a better view of the dominating mechanisms.

Figures 3(a) and (b) shows different EL transients recorded at different bias voltages in two samples, Spiro-a and Spiro-b, prepared with the layer stack m-TiO₂/MAPI/Spiro-OMeTAD,

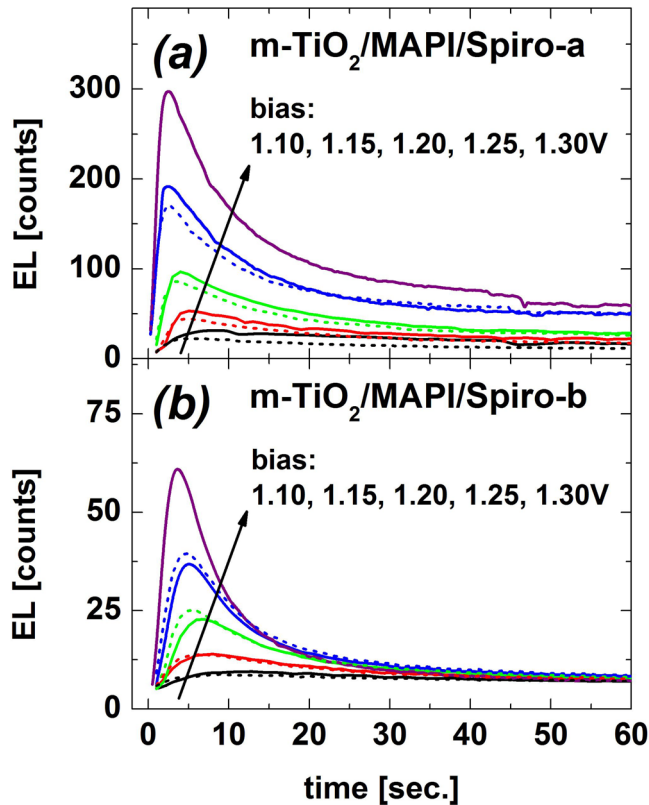


Figure 3. EL transients depending on bias voltage for two PSCs Spiro-a and Spiro-b for graphs (a) and (b), respectively. Both samples use the layer stack m-TiO₂/MAPI/Spiro-OMeTAD.

where full lines correspond to measurements with increasing voltage, starting from the lowest voltage (1.1 V) to the highest voltage (1.3 V), while dashed lines correspond to biasing voltages in decreasing direction (with the same voltage values as in the increasing direction). Between each measurement, 4 min rest with no polarization were allowed for the cells to reach equilibrium. Figures 3(a) and (b) show that higher bias voltages deliver higher EL_{MAX} as well as higher stationary values, due to the higher injected current (figure S4 in the SI shows the relation between EL_{MAX} and applied voltage). After the bias ramp-up, the cells do not seem to undergo significant degradation, as the transients recorded with decreasing bias follow very closely the original transients (dashed lines).

The applied bias not only affects the total EL value but it also shortens the transients, as shown in figure 4 where three characteristic times are plotted versus the applied voltage for the cells from figure 3. The times $t_{RISE50\%}$ and $t_{DEC50\%}$ correspond to the time that it takes the EL signal to rise and decay to 50% of its maximum value (EL_{MAX}), respectively. In addition, t_{MAX} is the transient peak time at EL_{MAX} . Since all three characteristic times tend to decrease with voltage, we conclude that biasing accelerates the involved fundamental processes mentioned above.

The behavior observed so far is also found in cells with different contact materials on the electron and hole transport layers (ETL and HTL, respectively). Figures 5(a) and (b) shows the EL transients for cells with two different contacts: cell (a) is prepared with CuPc as the HTL and cell (b)

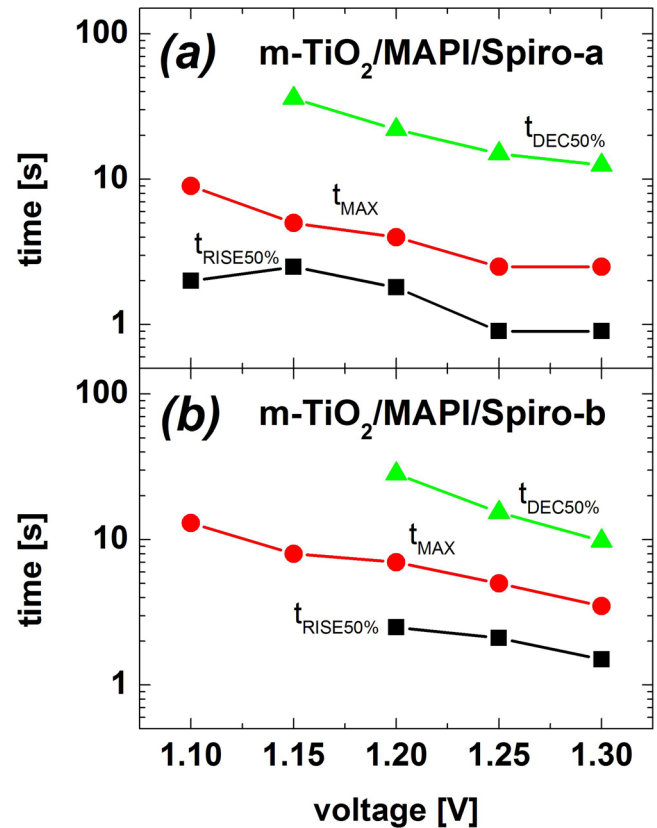


Figure 4. Three characteristic times in the EL transients of samples Spiro-a and Spiro-b as a function of bias voltage.

contains a planar (or dense) TiO₂ as the ETL. The overall EL trend observed for the previous samples also holds here: the EL reaches a peak in around 10 s to later decay towards a stationary intensity within 30–60 s. The sample containing CuPc as the HTL shows the slowest and weakest EL emission.

A comparison between all four samples is shown in terms of t_{MAX} in figure 6, showing that for a given polarization voltage, the slowest response is obtained by the sample with CuPc. We also notice that the sample with planar p-TiO₂ ETL shows intermediate times at comparable bias values. This suggests a stronger incidence of the HTL rather than the ETL on the EL transients, despite the large difference in effective interface area of the mesoporous compared to the planar TiO₂ layer.

Figure 7(a) shows the correlation between the value of EL_{MAX} and t_{MAX} for all cases. The highest EL_{MAX} values always correspond to the shorter t_{MAX} . A better quantitative comparison between the different cells is given in figure 7(b), where we define the quantum yield Q_e as the quotient between EL signal and current density J according to

$$Q_e(t) = EL(t)/J(t) \quad (1)$$

in units of counts/mA. In figure 7(b), the value for $Q_e(t_{MAX})$ is obtained from EL_{MAX} and the current density J_{MAX} at t_{MAX} . Here, we notice that the cells with higher Q_e correspond to the cells with higher open circuit voltages (V_{OC}) in table 1 as expected. High radiative recombination corresponds to low defect (i.e. non-radiative) recombination for a given number

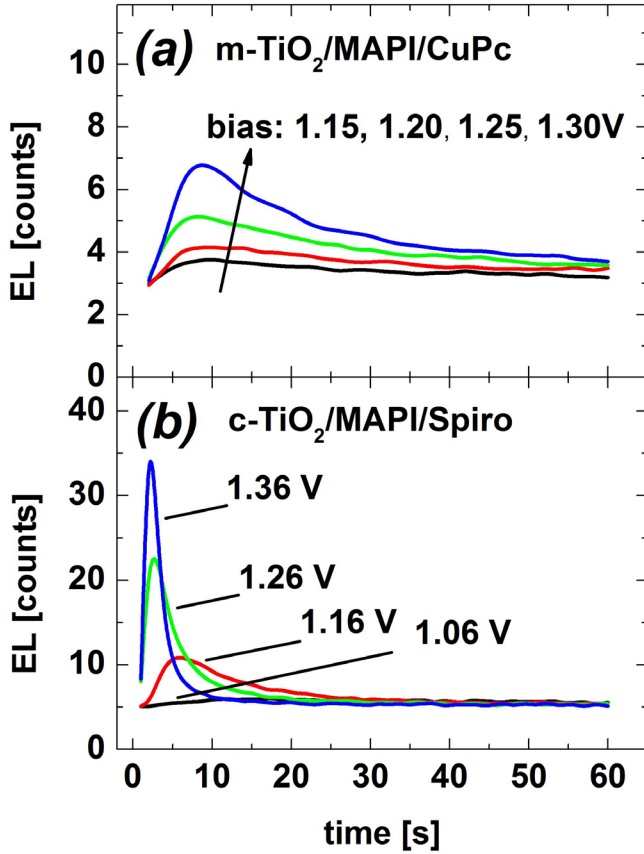


Figure 5. EL transients at different bias voltages observed for the sample with the layer stack m-TiO₂/MAPI/CuPc (a) and sample with compact TiO₂ in the stack p-TiO₂/MAPI/Spiro-OMeTAD (b).

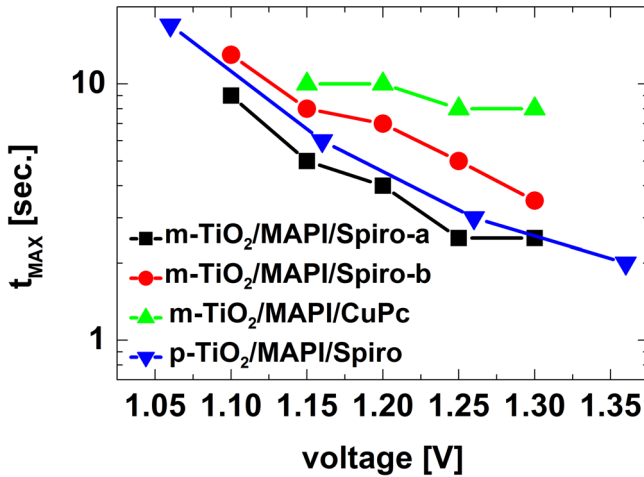


Figure 6. Evolution of t_{MAX} on bias voltage for the Spiro-OMeTAD (a) and (b), planar TiO₂ and the CuPc cells.

of injected carriers such that it necessarily results in increased EL and high V_{OC} . An identical trend is found for the stationary value of Q_e at each voltage (see below). A further correlation between the transient response and the solar cell performance is possible by recalling the results of t_{MAX} from figure 6. It can be noticed that cells with higher V_{OC} presents lower t_{MAX} , i.e. faster EL transients. This suggests that the dynamics of the EL response is linked to the amount of non-radiative recombination under stationary conditions, provided t_{MAX} relates to the

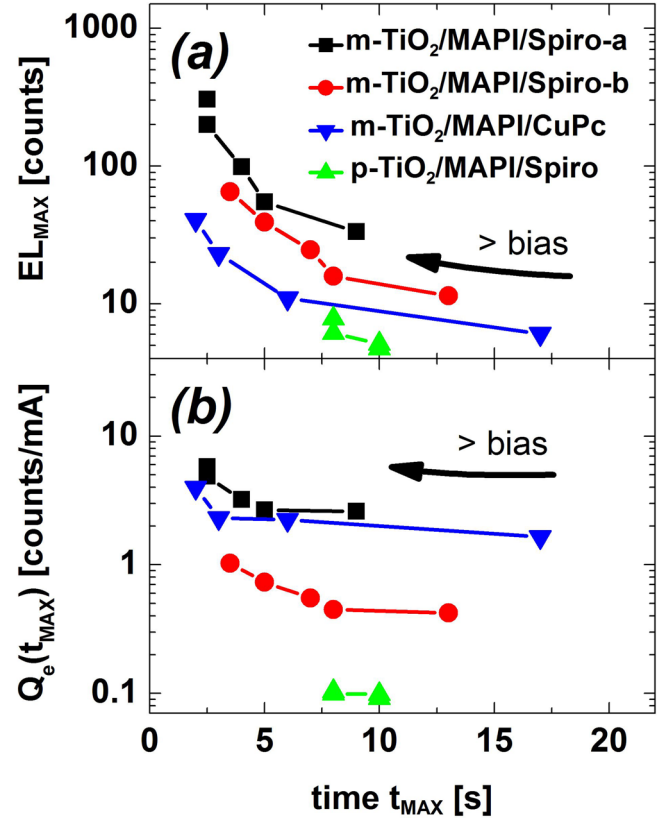


Figure 7. Comparison of EL_{MAX} (a) and $Q_e(t_{MAX})$ (b) as a function of t_{MAX} for the four samples.

time needed to overcome non-radiative interface recombination, which depends on the concentration of interface defects.

A further comparison is possible by relating the stationary quantum yield $Q_e(\infty)$ obtained with the values of EL and J at the end of the registered transients, and the steady state values of V_{OC} . According to the **electronic reciprocity principle for non-ideal solar cells**, steady state quantum yield and open circuit voltage are linearly related by [20]

$$V_{OC} = V_{OC,rad} + n_{rad} V_t \ln(Q_e), \quad (2)$$

where V_t is the thermal voltage, n_{rad} is the radiative ideality factor, and $V_{OC,rad} = 1.33$ V is the open-circuit voltage in the **radiative limit for MAPI** [21]. This equation assumes that the ratio between **radiative to total recombination is identical** under dark and illuminated characteristics, with the result that the same radiation is emitted from the device at a given voltage bias, regardless if it is a dark bias or V_{OC} . Applied to the devices studied here, figure 8 shows that $Q_e(\infty)$ correlates logarithmically to the open circuit voltage V_{OC} . The straight lines in figure 8 correspond to the fits of the values obtained from the m-TiO₂ cells at bias voltages $V = 1.15$ V (open symbols and dashed line) and at $V = 1.25$ V (filled symbols and full line), yielding $n_{rad} = 2.7$ and $n_{rad} = 2.1$, respectively. The solar cell based on p-TiO₂ cannot be included in the same fits as the m-TiO₂ cells because n_{rad} would change for a MAPI layer that is grown onto a different substrate since its crystallinity and optoelectronic properties are expected to depend on the underlayer material characteristics [22, 23].

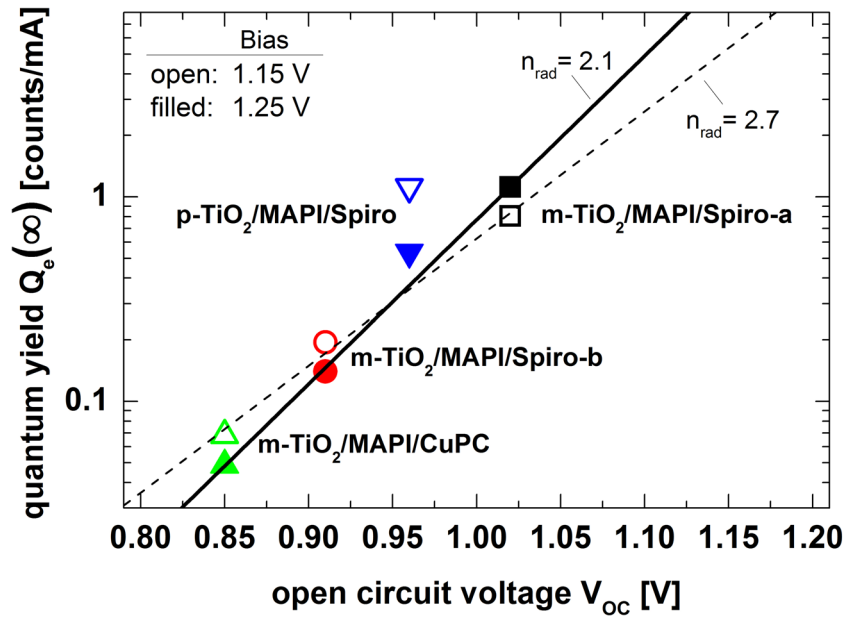


Figure 8. EL quantum yield in stationary conditions, $Q_e(\infty)$, versus the open circuit voltage V_{OC} of the different cells. Open/filled symbols correspond to applied voltage bias of 1.15 V/1.25 V, respectively. Fits with equation (2) are shown in lines.

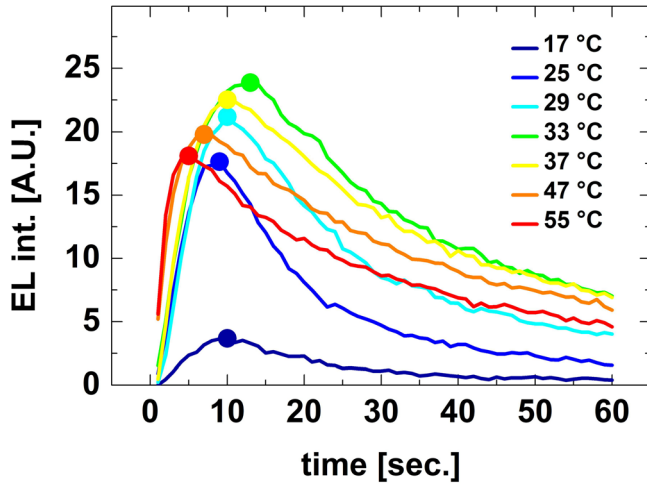


Figure 9. EL transients at a bias voltage of 1.3 V recorded under different temperatures (values indicated in legend) for a m-TiO₂/MAPI/Spiro-OMeTAD cell.

A similar validation of the optoelectronic reciprocity theory in MAPI solar cells was reported previously under stationary conditions by **correlation of spectral quantum efficiency and EL** [21]. The occurrence of radiative ideality factors higher than unity reflects the incidence of non-idealities, e.g. a high incidence of non-radiative recombination or the occurrence of radiative transitions between band tail energy states [20]. In amorphous Silicon solar cells, $n_{rad} > 2$ have been obtained and also shown to vary with bias level [24].

Since the **timescale of the observed EL transients is compatible with ionic diffusion and interfacial trapping/detrapping dynamics**, the EL transients are expected to show significant sensitivity to temperature changes. Figure 9 shows the obtained EL transients recorded at a bias voltage of 1.3 V between 17 °C and 55 °C for a m-TiO₂/MAPI/Spiro-OMeTAD solar cell. The temperatures are suggested by the color of each

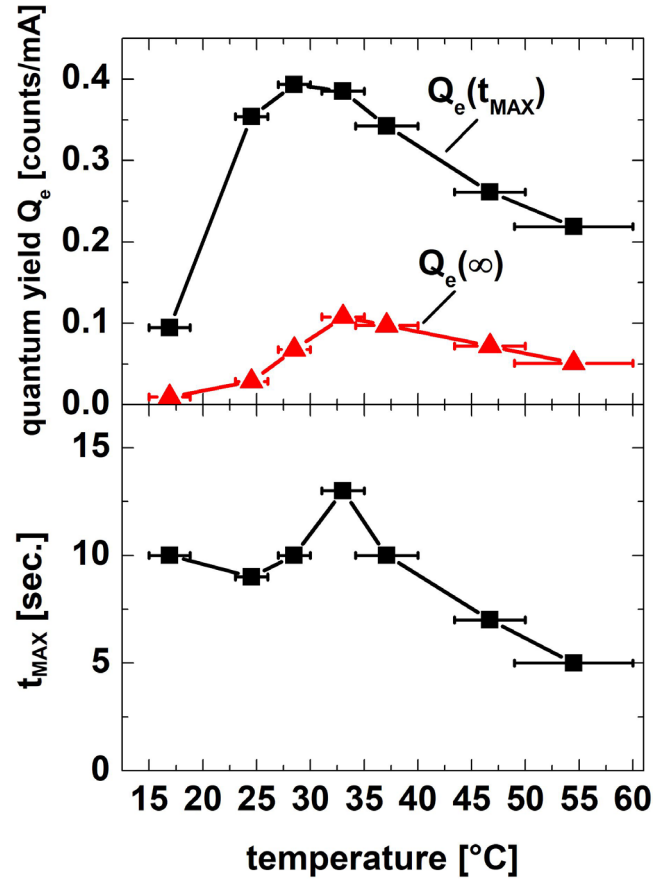


Figure 10. Temperature dependence of the quantum yield $Q_e(t_{MAX})$ and $Q_e(\infty)$ in stationary conditions (a). Time to reach maximum EL, t_{MAX} , versus temperature (b).

curve, from cold (blue) to hot (red). The maxima are indicated for clarity, showing that the EL first increases with increasing temperature to later decrease again above 33 °C. Since the current at each part of the EL transients increases

monotonously with temperature (see figure S5), it is the ratio of radiative to total recombination which must be changing with temperature.

The temperature dependence of EL can be better examined in terms of the quantum yields $Q_e(t_{MAX})$ and $Q_e(\infty)$ shown in figure 10(a), displaying maxima at 29 °C and 33 °C, respectively. Figure 10(b) also presents the t_{MAX} values as function of temperature with a peak at 33 °C. Although more experiments are needed to understand the observed behavior, we suggest that the observed maxima between 29 °C–33 °C could be related to a phase change that occurs in MAPI at 37 °C, where the crystal lattice changes from tetragonal to cubic [25] (other authors report the same phase change to occur between 42 °C and 57 °C, see [26, 27]). Around the peak seen in figure 10(b), t_{MAX} decreases with temperature, possibly owing faster ion dynamics and faster interface charge trapping/detrapping at higher temperatures. The phase change could introduce a retardation of the involved mechanisms, originating the peak in t_{MAX} .

4. Conclusions

EL measurements of solution-prepared one-step $\text{CH}_3\text{NH}_3\text{PbI}_3$ (MAPI) PSCs were recorded as a function of time, detecting a peak EL which depends on bias voltage, contact layer materials and temperature. The peaks are found at times in the 1 s–10 s range, while the whole transients last up to 60 s, suggesting that the involved mechanisms are likely governed by ion dynamics, e.g. originated in interface defect recombination and bulk defect generation by ion-vacancy generation. The characteristics of the transients are related to the open circuit voltage V_{OC} under solar illumination, showing that not only the stationary value but also the peak EL correlates with V_{OC} . The time required to reach the maximum EL holds an inverse relation to V_{OC} , possibly meaning that faster ion dynamics translates into better performing cells at bias voltages around or above V_{OC} . First temperature-dependent EL transient experiments show a maximum EL around 30 °C, close to the change of crystalline phase of MAPI at 37 °C. Further experiments in samples using different contact layers are planned to investigate if the observed maximum is strictly related to the phase change in MAPI or a consequence of interface properties. A possible technological implication of the observed non-monotonic behavior of EL with time and temperature is that the conventional use of EL imaging as a fast tool for diagnosing solar cells and modules requires caution when using MAPI devices prepared with traditional solution-processing techniques.

ORCID iDs

K Taretto  <https://orcid.org/0000-0003-2318-823X>

References

- [1] Battersby S 2019 News feature: the solar cell of the future *Proc. Natl Acad. Sci.* **116** 7–10
- [2] Snaith H J 2018 Present status and future prospects of perovskite photovoltaics *Nat. Mater.* **17** 372–6
- [3] Rajagopal A, Yao K and Jen A K-Y 2018 Toward perovskite solar cell commercialization: a perspective and research roadmap based on interfacial engineering *Adv. Mater.* **30** 1800455
- [4] Fuyuki T, Kondo H, Yamazaki T, Takahashi Y and Uraoka Y 2005 Photographic surveying of minority carrier diffusion length in polycrystalline silicon solar cells by electroluminescence *Appl. Phys. Lett.* **86** 262108
- [5] Helbig A, Kirchartz T, Schaeffler R, Werner J H and Rau U 2010 Quantitative electroluminescence analysis of resistive losses in Cu(In, Ga)Se_2 thin-film modules *Sol. Energy Mater. Sol. Cells* **94** 979–84
- [6] Kirchartz T, Helbig A, Pieters B E and Rau U 2011 Electroluminescence analysis of solar cells and solar modules *Advanced Characterization Techniques for Thin Film Solar Cells* ed D Abou-Ras et al (New York: Wiley) pp 61–80
- [7] Hameiri Z, Mahboubi Soufiani A, Juhl M K, Jiang L, Huang F, Cheng Y-B, Kampwerth H, Weber J W, Green M A and Trupke T 2015 Photoluminescence and electroluminescence imaging of perovskite solar cells *Prog. Photovolt., Res. Appl.* **23** 1697–705
- [8] Soufiani A M, Tayebjee M J Y, Meyer S, Ho-Baillie A, Sung Yun J, MacQueen R W, Spiccia L, Green M A and Hameiri Z 2016 Electro- and photoluminescence imaging as fast screening technique of the layer uniformity and device degradation in planar perovskite solar cells *J. Appl. Phys.* **120** 035702
- [9] Tress W, Marinova N, Moehl T, Zakeeruddin S M, Nazeeruddin M K and Grätzel M 2015 Understanding the rate-dependent J – V hysteresis, slow time component, and aging in $\text{CH}_3\text{NH}_3\text{PbI}_3$ perovskite solar cells: the role of a compensated electric field *Energy Environ. Sci.* **8** 995–1004
- [10] Sanchez R S, Gonzalez-Pedro V, Lee J-W, Park N-G, Kang Y S, Mora-Sero I and Bisquert J 2014 Slow dynamic processes in lead halide perovskite solar cells. Characteristic times and hysteresis *J. Phys. Chem. Lett.* **5** 2357–63
- [11] Wang H, Guerrero A, Bou A, Al-Mayouf A M and Bisquert J 2019 Kinetic and material properties of interfaces governing slow response and long timescale phenomena in perovskite solar cells *Energy Environ. Sci.* **12** 2054–79
- [12] Bandiello E, Ávila J, Gil-Escrig L, Tekelenburg E, Sessolo M and Bolink H J 2016 Influence of mobile ions on the electroluminescence characteristics of methylammonium lead iodide perovskite diodes *J. Mater. Chem. A* **4** 18614–20
- [13] Jaramillo-Quintero O A, Sanchez R S, Rincon M and Mora-Sero I 2015 Bright visible-infrared light emitting diodes based on hybrid halide perovskite with spiro-OMeTAD as a hole-injecting layer *J. Phys. Chem. Lett.* **6** 1883–90
- [14] Wong K K, Fakharuddin A, Ehrenreich P, Deckert T, Abdi-Jalebi M, Friend R H and Schmidt-Mende L 2018 Interface-dependent radiative and nonradiative recombination in perovskite solar cells *J. Phys. Chem. C* **122** 10691–8
- [15] Fantacci S, De Angelis F, Nazeeruddin M K and Grätzel M 2011 Electronic and optical properties of the spiro-MeOTAD hole conductor in its neutral and oxidized forms: a DFT/TDDFT investigation *J. Phys. Chem. C* **115** 23126–33
- [16] Ravishanker S, Almora O, Echeverría-Arrondo C, Ghahremanirad E, Aranda C, Guerrero A, Fabregat-Santiago F, Zaban A, Garcia-Belmonte G and Bisquert J 2017 Surface polarization model for the dynamic hysteresis of perovskite solar cells *J. Phys. Chem. Lett.* **8** 915–21
- [17] Wu B, Fu K, Yantara N, Xing G, Sun S, Sum T C and Mathews N 2015 Charge accumulation and hysteresis in

- perovskite-based solar cells: an electro-optical analysis *Adv. Energy Mater.* **5** 1500829
- [18] Li C, Guerrero A, Huettnner S and Bisquert J 2018 Unravelling the role of vacancies in lead halide perovskite through electrical switching of photoluminescence *Nat. Commun.* **9** 1–8
- [19] Wang M, Bian J, Feng Y, Zhang Y, Liu H and Shi Y 2018 Correlation of ETL in perovskite light-emitting diodes and the ultra-long rise time in time-resolved electroluminescence *Mater. Sci. Semicond. Process.* **80** 131–6
- [20] Rau U, Blank B, Müller T C M and Kirchartz T 2017 Efficiency potential of photovoltaic materials and devices unveiled by detailed-balance analysis *Phys. Rev. Appl.* **7** 044016
- [21] Tress W, Marinova N, Inganäs O, Nazeeruddin M K, Zakeeruddin S M and Graetzel M 2015 Predicting the open-circuit voltage of $\text{CH}_3\text{NH}_3\text{PbI}_3$ perovskite solar cells using electroluminescence and photovoltaic quantum efficiency spectra: the role of radiative and non-radiative recombination *Adv. Energy Mater.* **5** 1400812
- [22] Shi Y, Xing Y, Li Y, Dong Q, Wang K, Du Y, Bai X, Wang S, Chen Z and Ma T 2015 $\text{CH}_3\text{NH}_3\text{PbI}_3$ and $\text{CH}_3\text{NH}_3\text{PbI}_{3-x}\text{Cl}_x$ in planar or mesoporous perovskite solar cells: comprehensive insight into the dependence of performance on architecture *J. Phys. Chem. C* **119** 15868–73
- [23] Zhou Y, Vasiliev A L, Wu W, Yang M, Pang S, Zhu K and Padture N P 2015 Crystal morphologies of organolead trihalide in mesoscopic/planar perovskite solar cells *J. Phys. Chem. Lett.* **6** 2292–7
- [24] Müller T C M, Pieters B E, Kirchartz T, Carius R and Rau U 2012 Modelling of photo- and electroluminescence of hydrogenated microcrystalline silicon solar cells *Phys. Status Solidi c* **9** 1963–7
- [25] Milot R L, Eperon G E, Snaith H J, Johnston M B and Herz L M 2015 Temperature-dependent charge-carrier dynamics in $\text{CH}_3\text{NH}_3\text{PbI}_3$ perovskite thin films *Adv. Funct. Mater.* **25** 6218–27
- [26] Onoda-Yamamuro N, Matsuo T and Suga H 1990 Calorimetric and IR spectroscopic studies of phase transitions in methylammonium trihalogenoplumbates (II) *J. Phys. Chem. Solids* **51** 1383–95
- [27] Kawamura Y, Mashiyama H and Hasebe K 2002 Structural study on cubic-tetragonal transition of $\text{CH}_3\text{NH}_3\text{PbI}_3$ *J. Phys. Soc. Japan* **71** 1694–7